JOURNAL OF AIRCRAFT
Vol. 46, No. 6, November–December 2009

Heat Transfer and Pressure Measurements on a Thick Airfoil

Guoqiang Li* and Ephraim J. Gutmark†
University of Cincinnati, Cincinnati, Ohio 45221
and
Robert T. Ruggeri‡ and J. H. Mabe§
Boeing Phantom Works, Seattle, Washington 98108

DOI: 10.2514/1.44093

Knowledge of local heat transfer coefficients is essential to understanding and successful modeling of the ice accretion process on airfoils. Ice can change airfoil shape, alter the aerodynamic behavior, and impact aircraft performance and control. This paper reports measurements of local heat transfer coefficients (Frossling number) around a 28% thickness ratio airfoil covering 90% of both the top and bottom surfaces. Measurements were conducted at a constant wall temperature for angles of attack from −8.5 to 19.5 deg, freestream Mach numbers from 0.055 to 0.246, and chord Reynolds numbers from 2.5×10^5 to 10.85×10^5. Static pressures were measured simultaneously at the same operating conditions. The results show that the heat transfer coefficient starts high at the stagnation point, decreases with the developing laminar boundary layer, and then increases through a region of transition to a peak at the onset of the turbulent boundary layer. Thereafter, the heat transfer coefficient slowly decreases as the thickness of the turbulent boundary layer increases. The location of the onset of turbulence moves toward the leading edge on the top surface and toward the trailing edge on the bottom surface with increasing angle of attack at a constant Reynolds number. This transition is also affected by the Reynolds number. The measured surface static pressure coefficients provide additional evidence to the changing trend of the transition locations; that is, that the location where the abrupt jump in the Frossling number occurs closely coincides with the state change from a negative pressure gradient to a positive gradient.

Nomenclature

A = constant representing heat radiation loss and static measurements errors
C_p = pressure coefficient
c = chord length
F_r = Frossling number, $Nu/\sqrt{R_{eC}}$
$\bar{F}_r$ = average Frossling number
h = local convective heat transfer coefficient
k_a = air thermal conductivity
k_i = thermal conductivity of the airfoil base local to the tile i
M = Mach number, U/a
N_u = Nusselt number based on chord, hc/k
N_{ux} = local Nusselt number based on x, hx/k
Q = electrical heating power
R_{eC} = Reynolds number based on chord, Uc/ν
R_{ex} = local Reynolds number based on x, Ux/ν
T_{air} = air temperature
T_B = temperature of the airfoil base
T_i = temperature of the test tile
U = freestream velocity in the wind tunnel
X = distance from beginning of test section
x = distance from the leading edge along the chord
α = angle of attack

Subscript

i = heat element index

Presented as Paper 4202 at the 36th AIAA Thermophysics Conference, Orlando, FL, 22–26 June 2003; received 1 March 2009; revision received 30 August 2009; accepted for publication 31 August 2009.

*Research Assistant Professor, Department of Aerospace Engineering and Engineering Mechanics. Member AIAA.
†Distinguished Professor and Ohio Regents Eminent Scholar, Department of Aerospace Engineering and Engineering Mechanics. Fellow AIAA.
‡Associate Technical Fellow, Boeing Developmental Center, Mail Stop 4A-51. Member AIAA.
§Research Engineer, Boeing Developmental Center, P.O. Box 3707, Mail Stop 4A-51. Member AIAA.

I. Introduction

ICE accretion on airfoils poses a serious hazard for flight and can even cause aircraft loss at subsonic speed due to changing the airfoil shape, adding weight to the aircraft, reducing lift, and increasing drag [1]. Mullins et al. [2] reported severe drag increases of 300–400% in tests of two-dimensional flapped airfoils for angles of attack of ±6 deg. Smith et al. [3] tested a similar airfoil and observed a reduction of 40–60% in lift coefficient. To address ice accretion and anti-icing or de-icing, both experimental and numerical studies have been performed. Cebeci and Kafyeke [1] highlighted the key elements of ice accretion, including 1) ice accretion prediction, 2) ice system performance for anti-icing and de-icing, and c) icing effects on aircraft. They emphasized the importance of measuring heat transfer coefficients for validation of the ice prediction code. Prediction of the ice growth rates and the resulting shapes based on computational code are extremely sensitive to the heat transfer coefficients, because convective heat transfer is a prominent mechanism of the icing process and most computational schemes rely on empirical heat transfer relationships [4].

So far, most experimental measurements on heat transfer have concentrated on NACA symmetric airfoils. Gelder and Lewis [5] measured local heat transfer coefficients on a model NACA 65, 2-016 airfoil section along the chord with s/c (distance along the surface) covering the front 20% on the bottom surface and 60% on the top surface. Poinsatte [6] measured local heat transfer coefficients for a smooth NACA 0012 airfoil by using a steady-state heat flux method. The airfoil had a chord length of 0.533 m and a span length of 1.8 m. The measurements were performed around the leading edge from 8% s/c on the bottom surface to 8% on the top surface and over a range of chord Reynolds numbers of $R_{eC} = 1.2 \times 10^6$–2.5×10^6 at various angles of attack of up to 4 deg. The data showed that the Frossling number was greatest at the stagnation point and gradually decreased

to an average value of about 1 at $s/c = 0.083$. At zero angle of attack, the Nusselt number correlated well with the square root of the Reynolds number, but the data covered only a small region close to the leading edge and no heat transfer data were reported in the transition and turbulent regions. Poinsatte et al. [7] also reported heat transfer data measured on a roughened NACA 0012 airfoil. Artificial roughness was obtained by placing 2-mm-diam hemispheres in different patterns on the wing. The leading-edge roughening increased the heat transfer at the leading edge by only 10% over the smooth airfoil and did not affect the heat transfer downstream. Pais et al. [8] used a subsonic wind tunnel to measure the local convective heat transfer coefficients on a NACA 0012 airfoil in the range of $R_{eC} = 7 \times 10^5$–2×10^6. Local Nusselt numbers for the smooth airfoil were obtained for angles of attack $\alpha = 0$ to 8 deg. For $\alpha = 2, 4, 6$, and 8 deg, the average increase of Nusselt number on the top surface with respect to the bottom surface was 21, 36, 58, and 72%, respectively. These data show a strong dependence on angle of attack and suggest that heat transfer coefficients are substantially increased during the transition from laminar to turbulent boundary layer. Dukhan et al. [9] measured Frossling numbers for an ice-roughened NACA 0012 airfoil with $s/c = \pm 12\%$ and R_{eC} ranging from 4×10^5 to 1.6×10^6. His data for the same chord Reynolds number and at the same position on the airfoil showed that the Frossling number was generally higher on the roughened airfoil than for the smooth airfoil. The maximum increase was 51% for one rough glazelike ice horn case. Although all of these cases provided valuable information for understanding ice accretion and validating computational codes, few of these tests have measured heat transfer beyond 50% x/c and most covered only positive angles of attack. More importantly, the heat transfer coefficients change associated with transition from laminar to turbulent boundary-layer flow are rarely reported in the published literature.

Steady-state heat flux methods are commonly used for the measurement of local heat transfer coefficients on airfoils [4–9]. The method involves measuring the heat flux of a test tile that is usually heated electrically and instrumented with thermocouples. To minimize the heat loss to the body of the airfoil, the test tile is isolated from the surrounding part using heat-insulation material. In order to calculate the convective heat transfer from the electrical heat flow to the tile, the heat losses due to thermal radiation from the heated tiles to the surroundings and from conduction to the airfoil material have to be estimated. In the studies of NACA 0012 airfoil [4,6,7,9], the radiation heat loss was 0.5% based on the assumption of gray-body radiation and 0.05 emissivity of an aluminum test tile, and the conduction heat loss from the tiles to the surrounding bed was estimated to be 2%, based on the exact solution of two-dimensional conduction in a rectangular slab. An averaged uncertainty of 5.7% and maximum uncertainty of 7.8% were reported for heat transfer coefficients obtained in these studies.

Other techniques have also been used to obtain the heat transfer coefficient. Kestin and Wood [10] used the mass transfer analogy to deduce heat transfer coefficients from cylinders because accurate heat transfer measurements are difficult to obtain. They measured the mass transfer rate from cylinders and investigated the influence of the freestream turbulence level. The trend of the mass transfer coefficients over the entire measurement zone of 0–180 deg (including the stagnation point, the laminar, transitional, and turbulent regions) was similar to that of a thick airfoil. More recently, Henry et al. [11] used a laser heating method and infrared camera to measure heat transfer from airfoils.

The present study is motivated by the need for quality heat transfer data in the transition region of thick airfoils, which are commonly used for rotary-wing aircraft. It is also aiming to investigate the effects of freestream Mach number and angle of attack on the heat transfer coefficients within the transition region. By carefully addressing the uncertainty in calculating convective heat flux via calibration procedures, the present study provides heat transfer data on an asymmetric airfoil with a 28% thickness ratio. The effect of Reynolds number and angle of attack on the laminar–turbulent boundary-layer transition and heat flow are analyzed. Pressure coefficients are also measured in order to correlate the flowfield and heat transfer characteristics on this airfoil. The data presented include local Frossling number and pressure coefficient on the airfoil for five angles of attack and three Reynolds numbers. Compared with similar measurements in [5,6], the data presented in this study covers nearly the entire chord of the airfoil (from 90% bottom surface to 90% top surface).

II. Methodology

A. Experimental Setup

The heat transfer measurements were performed in the subsonic (maximum velocity $M = 0.3$) closed-circuit wind tunnel at the University of Cincinnati, Gas Dynamics and Propulsion Laboratory (Fig. 1). The test section of the wind tunnel has a cross section of 60.96 by 60.96 cm (2 by 2 ft), and it is 2.44 m (8 ft) in length. The wind tunnel is driven by a 240 hp ac motor with a two-stage variable-pitch fan. The motor speed is controlled by a Reliance frequency controller, and the fan pitch is controlled by a pneumatic actuator. A West 3800 controller maintains the air at a constant temperature in the wind tunnel. A pitot-static probe mounted upstream of the test section measures the static and total pressures that are used to calculate the freestream velocity.

Freestream velocity and the turbulence intensity in the wind tunnel were characterized by a calibrated single-element hot-film anemometer (A.A. Lab Systems, model AN-1005). Figure 2 shows the velocity, with error bars, measured at three different freestream velocities ($U = 20$, 44, and 59 m/s) and three different horizontal locations ($X = 43.2$, 102.9, and 190.5 cm) measured from the leading edge of the test section. The test wing was mounted at the $X = 183$ cm location, where the measured velocity matched the nominal speed with very small error (less then 1 m/s for 20 and 44 m/s, and 1.4 m/s for 59 m/s). The turbulence intensity is about 0.5% at 20 m/s, and 1% at 44 and 59 m/s, around the central vertical region, with less change along the horizontal direction.

The measured model is a BO28 airfoil having a chord of 20 cm (7.875 in.) and a span of 61 cm (24 in.) that was equipped with a series of heating tiles and thermocouples distributed circumferentially around the wing (Fig. 3). The wing was mounted horizontally on two circular plates that can rotate to any desired angle of attack (Fig. 4). The model is located 183 cm from the leading edge

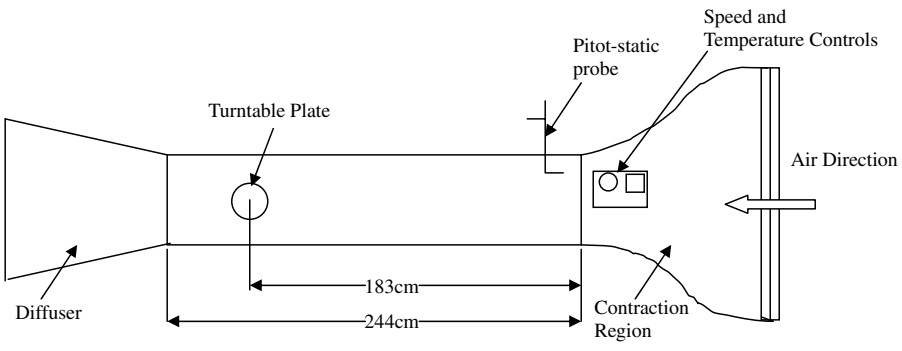

Fig. 1 Subsonic wind tunnel used for the heat transfer tests.

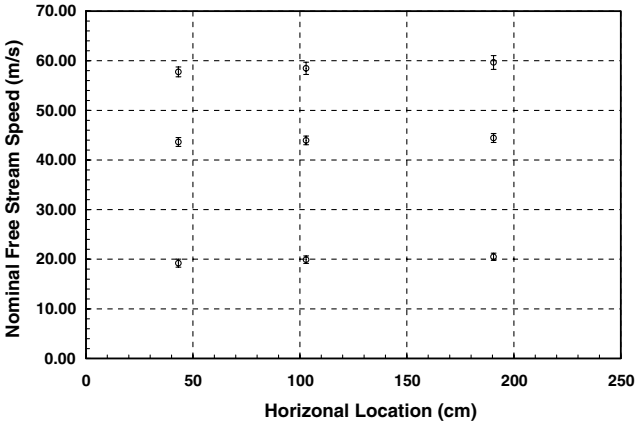

Fig. 2 Velocity measured by anemometer in the vertical central region of the wind tunnel at horizontal locations and three nominal freestream speeds; $U = 20$, 44, and 59 m/s; $x = 43.2$, 102.9, and 190.5 cm.

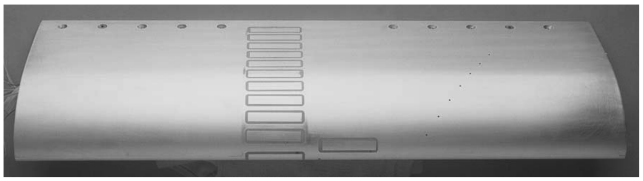

Fig. 3 BO28 wing of a rotary aircraft with arrangement of heat elements on the wing section.

of the test section, and it is centered vertically between the top and bottom walls of the wind tunnel, 30.48 cm from each.

The airfoil was equipped with 23 heated tiles [i.e., test tiles that are thermally isolated from the airfoil surface (Fig. 5)]. Four additional heater elements were used to control the airfoil temperature. The test tiles were individually heated and circumferentially distributed over the surface of the airfoil. Insulating epoxy and polyethylene foam surrounded each tile, insulating it from the surrounding airfoil. This construction minimized heat loss by conduction to and from the airfoil and allowed for accurate measurement of the heat being dissipated by each tile to the airstream. All of the heater elements could be operated in either constant-power mode, in which the power provided to the heating element was maintained constant, or

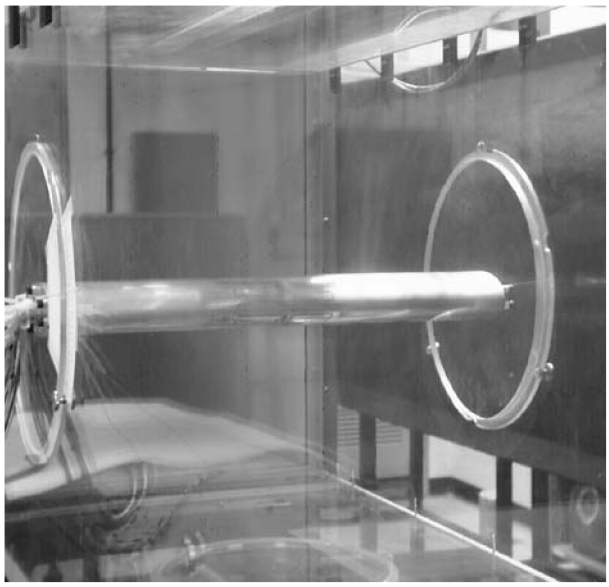

Fig. 4 Installation of the wing in the test section of the subsonic wind tunnel.

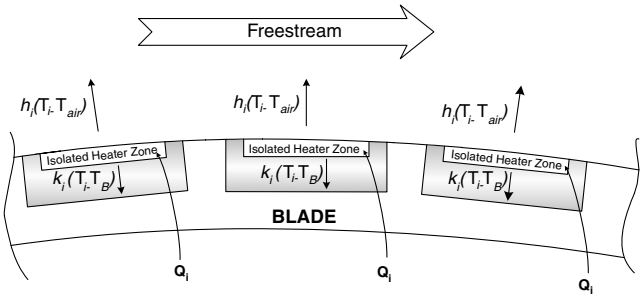

Fig. 5 Heat flow to and from isolated heater zones.

constant-temperature mode, in which the temperature of the tile was maintained constant. The constant-power mode was preferred for calibration purposes, whereas the constant-temperature mode was preferred for measuring local heat transfer coefficients. The freestream temperature was measured at two locations 15 cm (6 in.) upstream and downstream of the wing.

Calculation of the heat transfer coefficient for each isolated tile is based on a steady-state energy balance for a single tile, as shown in Eq. (1):

$$A_i + k_i(T_i - T_B) + h_i(T_i - T_{\text{air}})S_i = Q_i \tag{1}$$

where A_i is a constant, k_i is the thermal conductivity to the airfoil base, T_i is the temperature of the heating element $\boldsymbol{i}$, T_B is the temperature of the airfoil base, S_i is the surface area of the heating element $\boldsymbol{i}$, h_i is the local heat transfer coefficient, T_{air} is the temperature of the freestream air, and Q_i is the total heat produced by the ith resistance heater.

There are three types of heat transfer for each of the isolated heater zones: conduction from the heat element to the surrounding wing section through the insulating material, convection to the air, and radiation. The constant A represents all static measurement errors and radiative heat losses (which can be shown to be much smaller than convection). The conductive and convective terms have been shown experimentally to represent the major heat flows, and they are included explicitly.

A calibration procedure was applied before and after each test condition to determine the constant A and the conduction constant k. With the airfoil kept at the same temperature as the freestream air, a series of constant-power levels were applied to the isolated heater zones and steady-state data was obtained over a range of $T_i - T_B$ values. In the next step, the temperatures of the isolated heater zones were held constant, slightly above the temperature of the free airstream, and constant power was applied to the blade heaters while measuring the steady-state temperature difference $T_i - T_B$. In this way, heat flows dependent on the convective temperature difference $T_i - T_{\text{air}}$ and the conductive temperature difference $T_i - T_B$ were independently evaluated. A least-squares fit of the steady-state data to Eq. (1) was then used to calculate values for the A and k coefficients.

To investigate the possible error introduced by testing at different air temperatures and different temperature differentials between the heating elements and the air, a series of the tests were conducted at a constant freestream velocity of 20 m/s and 0 deg angle of attack. Figures 6 and 7 show the heat transfer coefficients for three different air temperatures (12, 17, and 21°C) and for three different differential temperatures between the heating elements and the freestream air (5, 10, and 15°C). These figures show that the influence of air temperature and of differential temperature on the measured heat transfer coefficients and on the locations of the transition points was negligible under the conditions of this test. This result was expected, because the local heat transfer coefficient is a function of the local flow speed, or Reynolds number, but not a strong function of temperature or temperature gradient. Based on these results, it was possible to choose one air temperature and temperature gradient to investigate the characteristics of heat transfer coefficients without introducing significant errors.

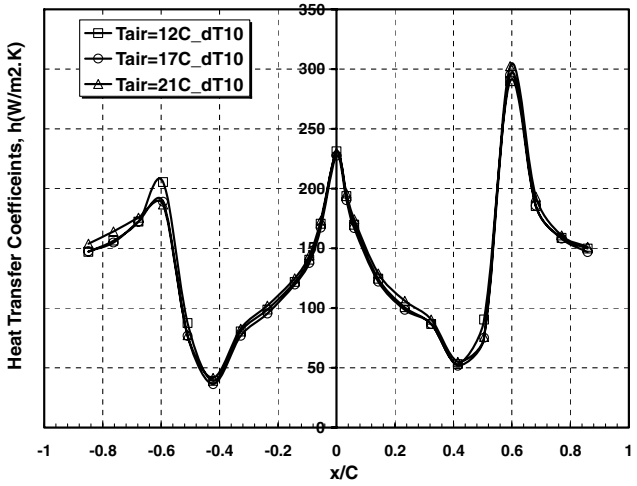

Fig. 6 Heat transfer coefficients for $T_{\text{air}} = 12$, 17, and 21°C at differential temperature gradient 10°C between the heating elements and the freestream air; $\alpha = 0$ and $U = 20$ m/s.

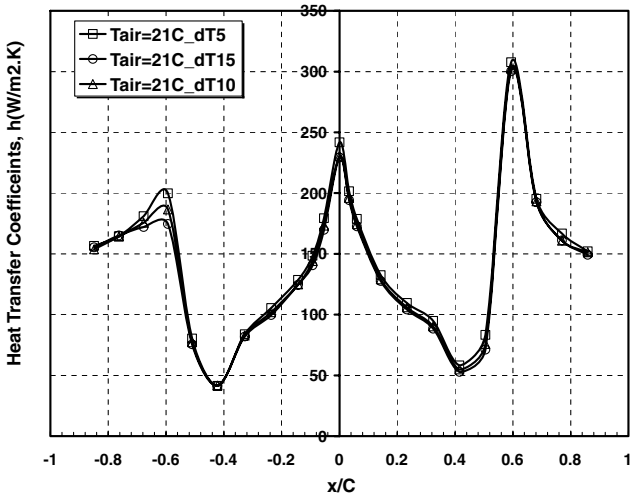

Fig. 7 Heat transfer coefficients for differential temperature gradient $\Delta T = 5$, 10, and 15°C at $T_{\text{air}} = 21$°C, $\alpha = 0$, and $U = 20$ m/s.

B. Test Procedure

For each test the airfoil was set up in the tunnel at a predetermined angle of attack. The airflow in the tunnel was started and allowed to stabilize at a predetermined velocity and temperature. The heater zones were then set to the same temperature as the airfoil. While keeping the gradient between the tiles and the airfoil ($T_i - T_B$) near zero throughout the whole test process by electrically controlling the tiles and the airfoil to the same temperature via separate heaters, a large temperature gradient ΔT was established between the airfoil and the freestream air. For all of the tests, the temperature gradient ΔT was set to 10°C. Data were taken when all of the heating elements reached thermal steady state, and then the values of A and k determined from the calibration procedure were combined with the test data to determine the value of the heat transfer coefficient h at that condition.

Heat transfer coefficients were measured for angles of attack ranging from −8.5 to +19.5 deg in 7 deg increments and at three Reynolds numbers: $R_{eC1} = 2.5 \times 10^5$, $R_{eC2} = 5.8 \times 10^5$, and $R_{eC3} = 10.85 \times 10^5$. The Reynolds number $R_{eC} = U \cdot c/\nu$ was defined using the chord length c, the wind tunnel velocity U, and the kinematic viscosity ν. The calibration procedure was repeated twice for each Reynolds number, once before and again after the data was acquired for a set of angles of attack. Testing at each air speed was completed within one day to ensure that both calibrations were consistent with the data taken that day.

C. Pressure Coefficients

Fifteen static pressure taps were circumferentially distributed over the surface of the airfoil. Differential static pressure (relative to far upstream pressure) was scanned by a type J Scanivalve system. These differential static pressure data along with the dynamic pressure that was measured by a pitot tube were used to calculate the pressure coefficients C_p, defined as

$$C_p = \frac{p_s - p_\infty}{p_d} \tag{2}$$

where $p_s - p_\infty$ is the differential static pressure, and p_d is the dynamic pressure.

D. Error Analysis

Uncertainty analysis was performed based on Eq. (1). Experimental observation and numerical evaluation of results indicates that the heat flows represented by the A term and the conduction term contribute no significant errors to the result. Therefore, the A and $ki(Ti - T_B)$ terms have been ignored in the uncertainty analysis. The simplified form of Eq. (1) is

$$h_i(T_i - T_{\text{air}})S_i = Q_i \tag{3}$$

Also,

$$Q_i = U_i \times I_i \tag{4}$$

where U_i is the voltage and I_i is the current through the ith heater element.

The convective heat transfer coefficient is expressed as

$$h_i = \frac{U_i I_i}{(T_i - T_{\text{air}})S_i} \tag{5}$$

where h_i has the unit of $\text{W/K} \cdot \text{m}^2$. The error from area S_i can be neglected in this formula.

Therefore, the total uncertainty (in terms of relative error) for the heat transfer coefficients can be expressed (according to the formula from Moffat [12]) as

$$\frac{\delta h}{h} = \sqrt{\left[\frac{\delta(T_i - T_{\text{air}})}{T_i - T_{\text{air}}}\right]^2 + \left[\frac{\delta I}{I}\right]^2 + \left[\frac{\delta U}{U}\right]^2} \tag{6}$$

There are three main sources of errors: 1) temperature measurements, 1% from type K thermocouples (based on an accuracy of 0.1 and 10°C temperature gradient); 2) voltage fluctuations, 5.1% based on measured differences between set point and applied values; and 3) current fluctuation, 5.1% based on average of measured current during the test. Therefore, the main error source is the heating power system, and the total error is approximately 7.3%.

The error of pressure coefficient is estimated based on the accuracy of differential static pressure and dynamic pressure from formula (2). The pressure transducers of both pressure measurements have accuracy of 0.5%, therefore introducing 0.7% error of pressure coefficient.

III. Results and Discussion

A. Heat Transfer Coefficients

Based on the surface convective heat transfer coefficients from Eq. (1), the local Nusselt number N_{ui} and Frossling number F_{ri} were calculated using Eqs. (7) and (8):

$$N_{ui} = \frac{h_i x}{k_a} \tag{7}$$

$$F_{ri} = \frac{N_{ui}}{\sqrt{R_{eC}}} \tag{8}$$

The Frossling numbers along the airfoil chord are shown in Figs. 8a–8c for three Reynolds numbers. The negative x axis

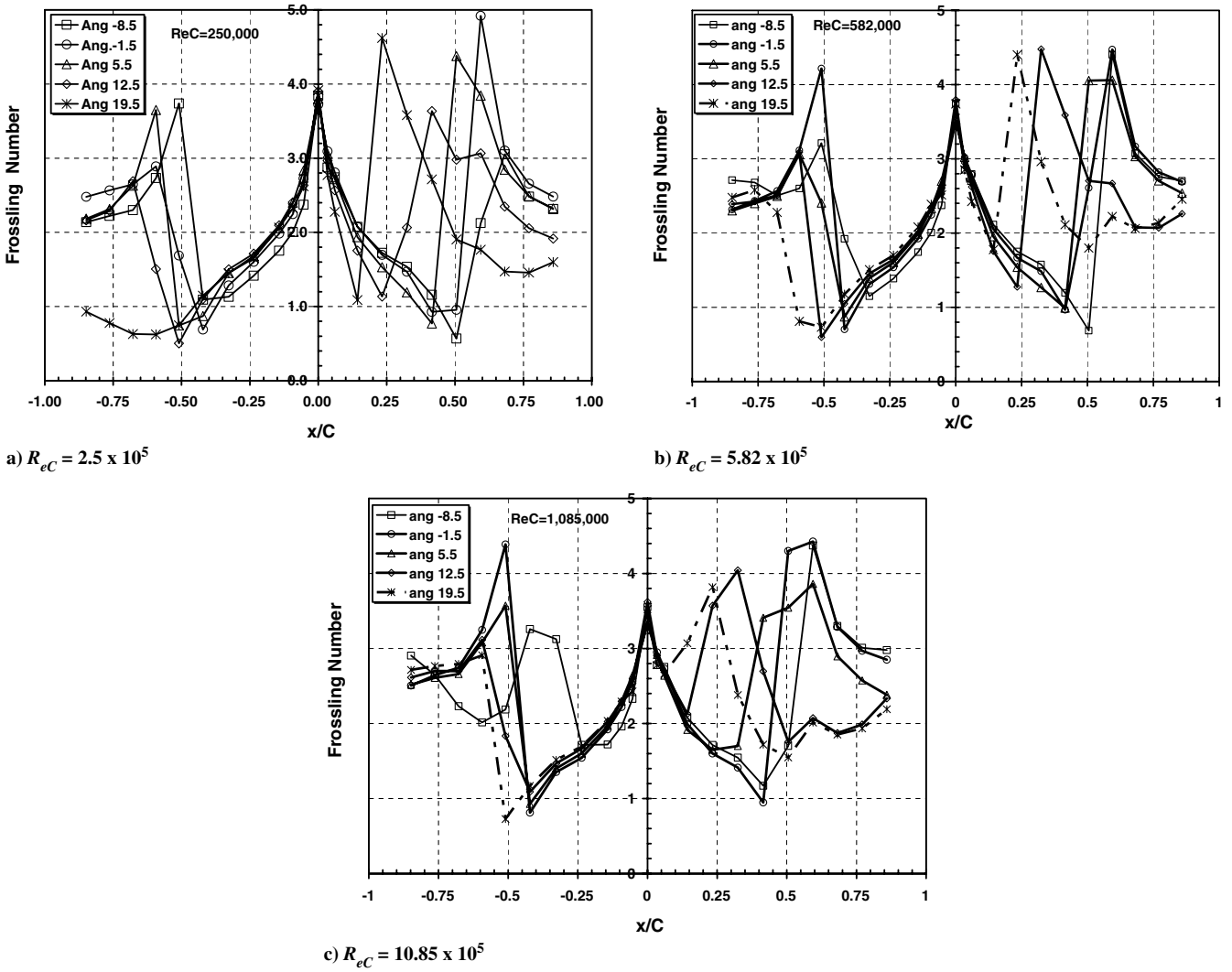

Fig. 8 Frossling number vs x/c on the BO28 airfoil at different angles of attack: a) $R_{eC} = 2.5 \times 10^5$ and $M_a = 0.055$, b) $R_{eC} = 5.8 \times 10^5$ and $M_a = 0.128$, and c) $R_{eC} = 10.85 \times 10^5$ and $M_a = 0.246$.

represents the bottom surface and the positive x axis represents the top surface. Using the plot for $R_{eC} = 250,000$ and $a = -1.5$ deg as an example, the typical behavior of the F_r is shown as follows:

1) On the bottom surface, F_r starts with a high value (close to 4) at the stagnation point on the leading edge (at $x/c = 0$), decreases to 1 at the initiation point of transition from laminar to turbulent flow, jumps abruptly to a high value, and then drops again toward the trailing edge.

2) On the top surface, F_r changes in a similar manner, but the transition to turbulent flow may occur at a different location and the abrupt jump after transition can have a higher magnitude.

It should also be noted that significant heat transfer enhancement results from the transition, which can be up to six times higher than the minimum value as observed from the curves for $\alpha = -1.5$ at $R_{eC} = 5.8 \times 10^5$ and 10.85×10^5. Although the typical shapes of F_r curves are similar for different angles of attack, there are obvious differences in the locations of transition. As observed from Figs. 8a–8c, the transition from laminar to turbulent flow was dramatically affected by the angle of attack. The transition locations move toward the leading edge on the top surface and move toward the trailing edge on the bottom surface with increasing angle of attack from −8.5 to 19.5 deg for all three Reynolds numbers tested. With a large angle of attack (19.5 deg) at the lower Reynolds number ($R_{eC} = 250,000$), the transition on the lower surface cannot be identified for this case from the plot in Fig. 8a. To clarify this behavior, the variation of the transition locations versus angle of attack is plotted in Fig. 9 for the three Reynolds numbers. The y axis is the x/c with positive as the top surface and negative as the bottom surface. On the top and the bottom surfaces, the transition location from laminar to turbulence flow has opposite trends with the angle of attack, approaching the leading edge on the top surface while approaching trailing edge on the bottom surface.

In this study, the Reynolds numbers also affect the location of transition and the magnitude of the F_r at the transition location,

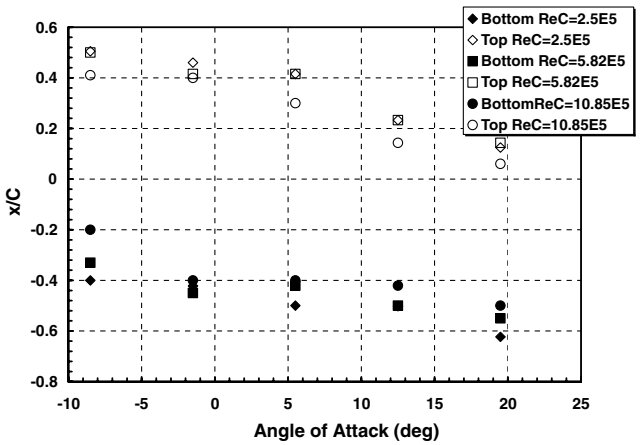

Fig. 9 Transition locations versus angle of attack at different Reynolds numbers; $R_{eC} = 2.5 \times 10^5$–10.85×10^5.

contrary to Gelder and Lewis [5] observation that an increase of airspeed from 61.3 to 86.2 m/s had no measurable effect on the location of the minimum convective heat transfer, which remained at 8% chord. This phenomenon is more obvious for large negative and positive angles of attack. As shown in Fig. 10, high Reynolds number moves the transition from laminar to turbulent flow toward the leading edge and increases the F_r at the transition location. For example, the F_r at transition on the top surface of $\alpha = 19.5$ are 1, 1.7, and 2.7 for $R_{eC} = 2.5 \times 10^5$, $5.8 \times 10_5$, and 10.85×10^5, respectively. This early transition at higher Reynolds numbers elevates the $\bar{F}_r$. This trend was observed for all angles of attacks in this study as shown in Fig. 10 and is summarized in Fig. 11, which shows the plots

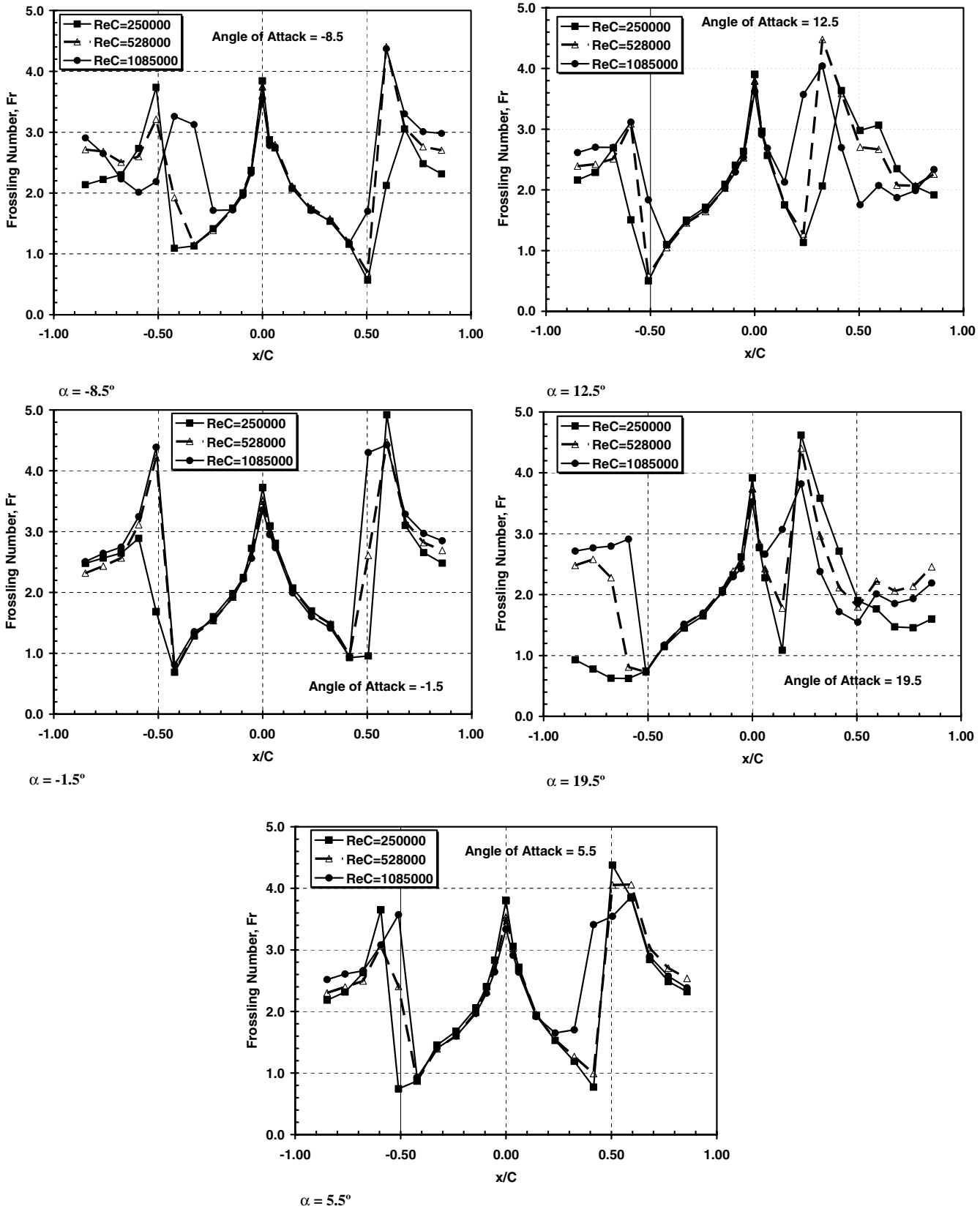

Fig. 10 Frossling number vs x/c on the BO28 airfoil at different Reynolds numbers.

of transition location x/c versus Reynolds number. It is also noticed that the averaged heat transfer coefficient is generally higher on the top surface than on the bottom surface as shown in Fig. 12. On the top surface, $\bar{F}_r$ decreases when the angle of attack becomes either large positive or large negative. On the bottom surface, however, $\bar{F}_r$ decreases with increasing of angle of attack. It was also observed from Fig. 10 that for different Reynolds numbers at the same angle of attack, the Frossling numbers are almost identical for all three Reynolds numbers in the laminar flow region before the transition point. This holds true for all angles of attack, suggesting that F_r is a good similarity parameter for the heat transfer characteristics at different angles of attack. However, after the transition point, the F_r shows different trends with the Reynolds number, as expected.

The F_r at the stagnation point is in the range of 3.5–3.9 for angle of attack $\alpha = -8.5$–19.5 and $R_{eC} = 2.5$–10.85×10^5 (Figs. 8a–8c), indicating that the F_r at the stagnation point is mostly affected by the impingement of freestream air and is less dependent on the angle of attack and Reynolds number. In the region of $\pm 5\%$ x/c around the stagnation point, the F_r varies with the angle of attack on almost the same curve, a strong indication of similarity of heat transfer in this laminar boundary-layer region.

B. Pressure Coefficient *Cp*

The transition from laminar to turbulent flow was also evidenced from the pressure coefficient distribution on the airfoil surface. Static pressure was measured in the range of 7–60% of the chord on the top surface and 7–65% of the chord on the bottom surface along with the heat transfer coefficients. Figure 13 shows the static pressure coefficient on the top and bottom surfaces of the BO28 at $R_{eC} = 2.5$ to 10.85×10^5 and $\alpha = -8.5$ to 12.5. The Cp curves for different Reynolds numbers collapse together for most angles of attack, except on the top surfaces at the highest angles of attack: $\alpha = 12.5$ and 19.5 deg. At the highest angle of attack ($\alpha = 19.5$ deg) and low Reynolds number, the boundary-layer growth on the top surface causes the C_p to deviate from the regular trend.

To reveal the correlation between the C_p and the location of transition from laminar to turbulent flow, the C_p variation with x/c was tracked on the top and bottom surfaces separately. Taking the C_p curves for $\alpha = -8.5$ as an example, it was possible to observe that Cp decreases gradually up to $x/c = 0.42$ and then increases. Starting from this point, the downstream pressure is higher than upstream pressure and an adverse pressure gradient is established. The point starting to have adverse pressure gradient at $x/c = 0.42$ is coincident with the location of transition from the laminar to turbulence flow, as identified in Fig. 9 for this angle of attack. Similar observations were also made for $\alpha = -1.5$ and 5.5, where the adverse pressure gradients on the top surface start earlier with higher angle of attack. Therefore, on the top surface, the establishment of adverse pressure gradient moves toward the leading edge when angle of attack increases and promotes earlier laminar–turbulent transition. Accordingly, on the bottom surfaces, the adverse pressure gradients starting points are delayed by the increment of angle of attack, thus delaying the transition locations toward the trailing edge.

At the highest angles of attack of $\alpha = 12.5$ and 19.5 deg, the Cp is a constant value at the aft section of the airfoil, indicating flow separation. This resulted in reduced F_r at these locations relative to the lower-angle-of-attack cases.

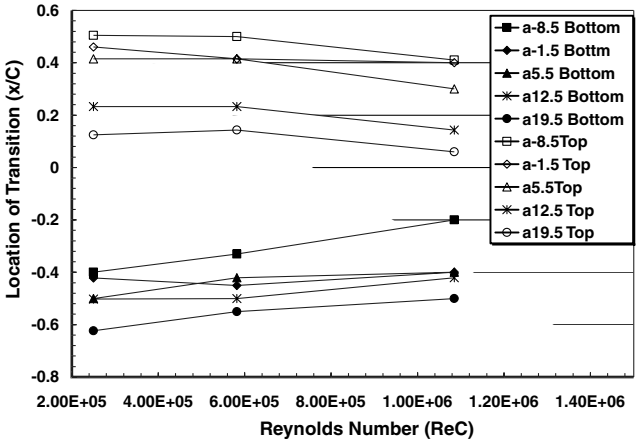

Fig. 11 Locations of transition in heat transfer versus Reynolds number for different angles of attack.

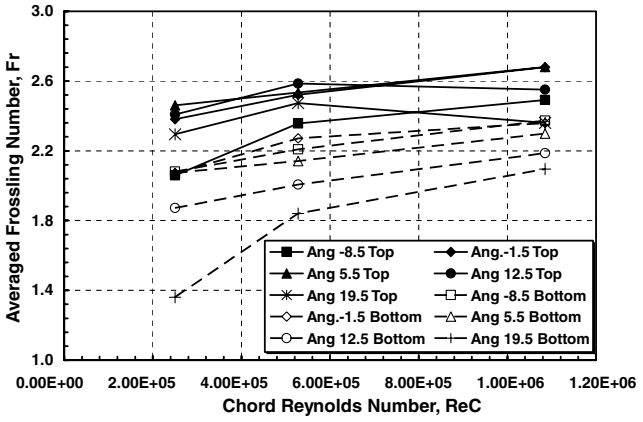

Fig. 12 Averaged Frossling numbers on the top and bottom surfaces at different Reynolds numbers and angles of attack of the BO28 airfoil.

C. Discussion

As shown in the previous section, the transition from laminar to turbulent flow has significant impact on the local heat transfer coefficient and strongly correlates with the Reynolds number and the local pressure distribution. BO28 is an airfoil with a ratio of maximum thickness to chord length of 28%, which is 2.5 times and 1.75 times the wing thickness ratio of the NACA 0012 and NACA 65, 2-016 airfoils tested in airfoil icing studies [5–7]. Analytically, the local Nusselt numbers on a flat plate at zero angle of attack for laminar [Eq. (9)] and turbulent [Eq. (10)] flows are given by [12]

$$Nu_x = 0.332 Pr^{1/3} R_{ex}^{1/2} \tag{9}$$

$$Nu_x = 0.029 Pr^{0.4} R_{ex}^{0.8} \tag{10}$$

Here, the local Reynolds number is defined as

$$R_{ex} = \frac{Ux}{v} \tag{11}$$

Figure 14 shows the correlation of the local Nusselt number versus the local Reynolds number as well as analytical solutions for a flat plate at zero angle of attack. On the log-scale plot, the Nu_x linearly increases with Re_x, but has much higher magnitude than the value predicted from flat-plate laminar solution. Similarly, in the turbulent flow region, measured Nu_x was greater than the flat-plate prediction. The shape of this airfoil causes significant variation of the heat transfer coefficients relative to predictions for a flat plate, and it would therefore be problematic to predict the heat transfer coefficients of this fairly thick airfoil using flat-plate values.

Another important observation to point out is the dependence of $(\bar{F}_{r_{\text{top}}} - \bar{F}_{r_{\text{bottom}}})/\bar{F}_{r_{\text{bottom}}}$, the relative increase in averaged Frossling number on the top surface with respect to the bottom one, as a function of the angle of attack. Figure 15 plots the percentage increase in Frossling number for $R_{eC} = 2.5$ to 10.85×10^5 and compares it with Pais et al. [8] data for a NACA 0012 airfoil. For $R_{eC} = 2.5$ to 5.8×10^5, at positive angles of attack, $(\bar{F}_{r_{\text{top}}} - \bar{F}_{r_{\text{bottom}}})/\bar{F}_{r_{\text{bottom}}}$ is almost linearly dependent on the angle of attack, but with a much smaller slope compared to the thinner airfoil NACA 0012. For $R_{eC} = 10.85 \times 10^5$, the flow separation on the top surface

at high angles of attack, such as $\alpha = 12.5$ and 19.5, yields different behavior of the local heat transfer, and the overall trend is quite different from the linear curve.

IV. Conclusions

The present study of heat transfer coefficients and pressure coefficients on an asymmetric airfoil provides a new database for understanding the flow and heat transfer behavior on thick airfoils. The carefully controlled heat flux via electrical heating elements approach and the calibration and test procedures ensure the data quality.

In the region of the laminar boundary layer, which extends from the stagnation point to the start of transition, the Frossling numbers vs x/c at a given angle of attack collapse on the same curve for all of the Reynolds numbers, following the same trends of decrease from the stagnation point to the transition location. However, the transition locations are dependent on angle of attack and Reynolds number. The transition location tends to move toward the leading edge on the top surface and toward the trailing edge on the bottom surface when the angle of attack increases. This trend remains the same for all

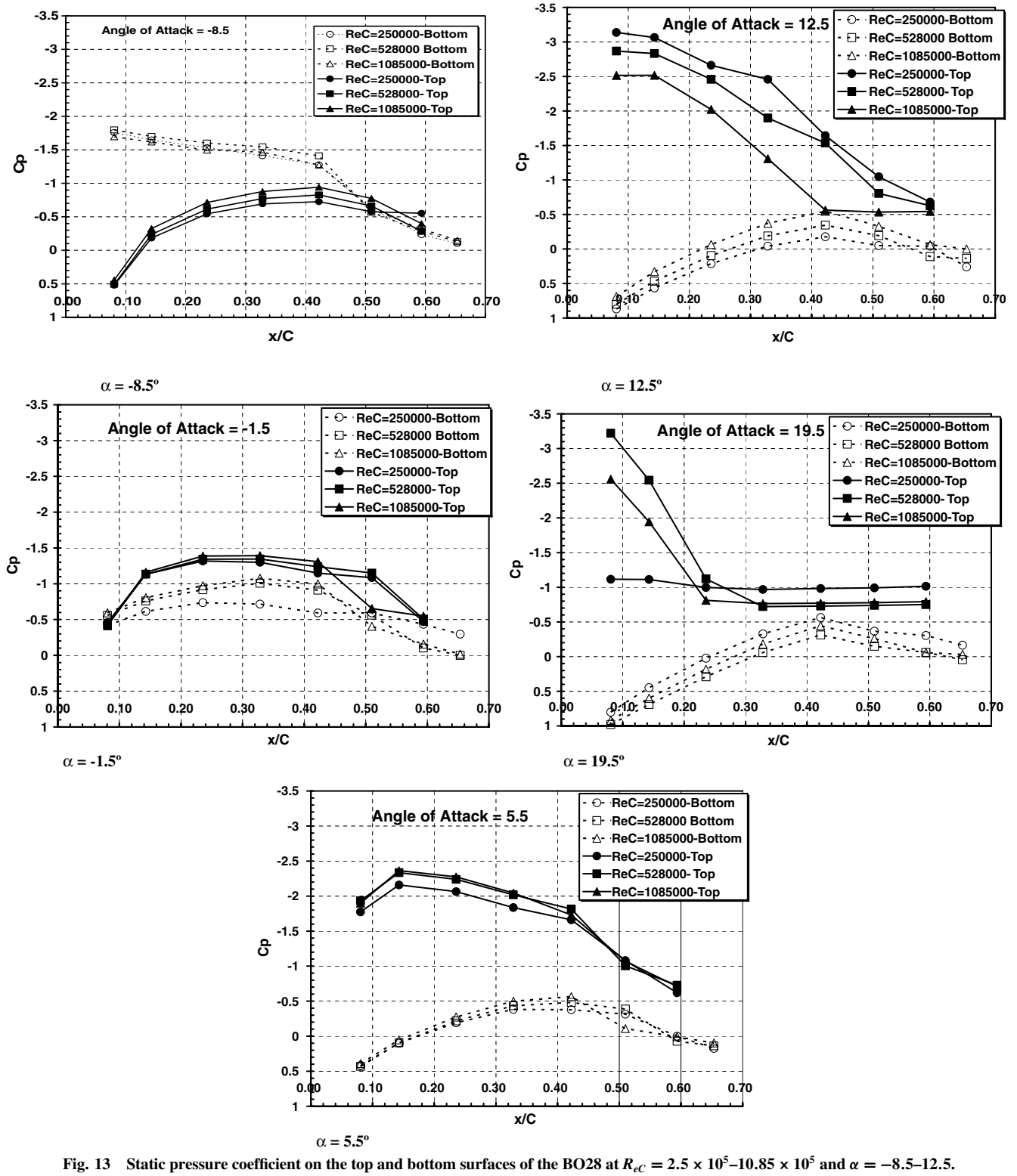

Fig. 13 Static pressure coefficient on the top and bottom surfaces of the BO28 at $R_{eC} = 2.5 \times 10^5$–10.85×10^5 and $\alpha = -8.5$–12.5.

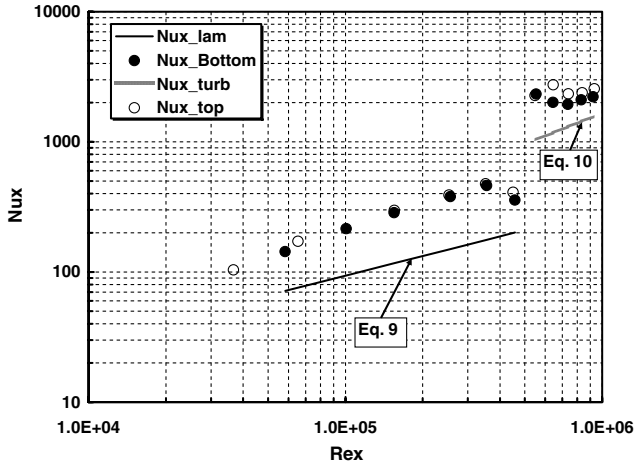

Fig. 14 Correlation of Nusselt number versus local Reynolds number for $\alpha = -1.5$ and 10.85×10^5.

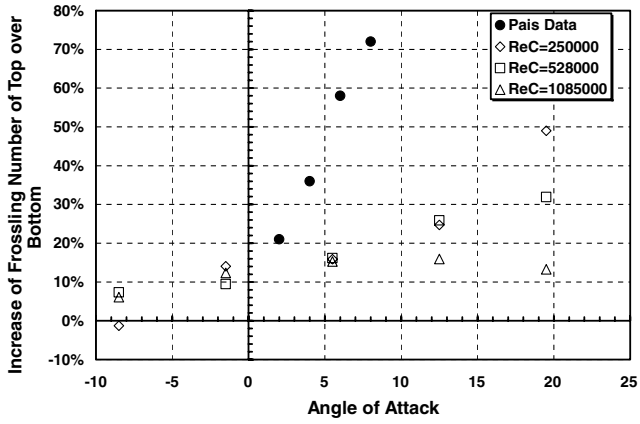

Fig. 15 Dependence of increase of Frossling number on the top surface with respect to the bottom surface on the angle of attack at $R_{eC} = 2.5 \times 10^5$–10.85×10^5. Pais et al. data are from [8].

three Reynolds numbers. Following transition, the heat transfer coefficients, which initially increase substantially, start to decrease as the turbulent boundary layer grows. High Reynolds numbers also promote early transition, which results in greater averaged Frossling numbers. It should be noticed that the transition location was not significantly influenced by the temperature gradient between the airfoil and the air within the tested flow range.

The evolution of the boundary layer on the airfoil surface correlates with changes in the heat transfer coefficient. The abrupt increase in the Frossling number signals the transition from laminar to turbulent flow, where the pressure gradient changes from favorable to adverse. The trend of the variation of heat transfer coefficients along x/c is consistent with the known observation that the location at which the adverse pressure gradient begins moves toward the leading edge on the top surface and toward the trailing edge on the bottom surface when angle of attack increases.

Compared with a thinner airfoil such as NACA 0012, the BO28 exhibits significant deviation from the solution of a flat plate and requires special consideration in numerical simulation.

References

[1] Cebeci, T., and Kafyeke, F., "Aircraft Icing," *Annual Review of Fluid Mechanics*, Vol. 35, 2003, pp. 11–21. doi:10.1146/annurev.fluid.35.101101.161217.

[2] Mullins, B., Jr., Smith, D., and Korkan, K., "Effect of Icing on the Aerodynamics of a Flapped Airfoil," AIAA Paper 95-0449, Jan. 1995.

[3] Smith, D., Mullins, B., Jr., and Korkan, K., "Effect of Icing on the Aerodynamic Performance of a Series of Two Dimensional Airfoils at Low Reynolds Numbers," AIAA Paper 95-0453, Jan. 1995.

[4] Dukhan, N., De Witt, K. J., Masiulaniec, K. C., and Van Fossen, G. J., Jr., "Experimental Frossing Numbers for Ice-Roughened NACA 0012 Airfoil," *Journal of Aircraft*, Vol. 40, No. 6, 2003, pp. 1161–1167. doi:10.2514/2.7205

[5] Gelder, T. F., and Lewis, J. P., "Comparison of Heat Transfer From Airfoil in Natural and Simulated Icing Conditions," NACA TN-2480, 1951.

[6] Poinsatte, P. E., "Heat Transfer Measurement from a NACA 0012 Airfoil in Flight and in the NASA Lewis Icing Research Tunnel," NASA CR-4278, 1990.

[7] Poinsatte, P. E., Van Fossen, G. J., Newton, J. E., and De Witt, K. J., "Roughness Effect on Heat Transfer of a NACA 0012 Airfoil," *Journal of Aircraft*, Vol. 28, No. 12, 1991, pp. 908–911. doi:10.2514/3.46116

[8] Pais, M., Singh, S., and Zou, L., "Determination of Local Heat Transfer Characteristic on Simulated Smooth Glaze Ice Accretions on a NACA 0012 Airfoil," AIAA Paper 88-0292, Jan. 1988.

[9] Dukhan, N., De Witt, K. J., Masiulaniec, K. C., and Van Fossen, G. J., Jr., "Experimental Heat Transfer Coefficients from Ice-Roughened Surfaces for Aircraft de-icing Design," *Journal of Aircraft*, Vol. 36, No. 6, 1999, pp. 948–956. doi:10.2514/2.2556

[10] Kestin, J., and Wood, R. T., "The Influence of Turbulence on Mass Transfer from Cylinders," *Journal of Heat Transfer*, Vol. 93, Nov. 1971, pp. 321–327.

[11] Henry, R. C., Guffond, D., Garnier, F., and Bouveret, A., "Heat Transfer Coefficient Measurement on Iced Airfoil in Small Icing Wind Tunnel," *Journal of Thermophysics and Heat Transfer*, Vol. 14, No. 3, 2000, pp. 348–354. doi:10.2514/2.6551

[12] Moffat, R. J., "Describing the Uncertainties in Experimental Results," *Experimental Thermal and Fluid Science*, Vol. 1, No. 1, 1988, pp. 3–17. doi:10.1016/0894-1777(88)90043-X